

# Reentrant superconductivity and Stoner boundaries in twisted WSe<sub>2</sub>

Lauro B. Braz<sup>1</sup> and Luis G. G. V. Dias da Silva<sup>1</sup>

<sup>1</sup>*Instituto de Física, Universidade de São Paulo,  
Rua do Matão 1371, São Paulo, São Paulo 05508-090, Brazil*

(Dated: January 21, 2026)

We investigate spin–valley instabilities and their connection to the reentrant superconducting states recently observed in the twisted bilayer dichalcogenide WSe<sub>2</sub> at a 5° twist angle. Starting from an effective three-orbital faithful Wannier model for the spin-locked moiré bands, combined with orbital-dependent Hubbard interactions, we analyze the evolution of magnetic instabilities as a function of carrier density using the matrix random phase approximation (mRPA) approach. By computing the Stoner boundary lines from the spin–valley susceptibilities over the electric-field by hole filling phase diagram, we show that the spin–valley instabilities result in ordered states in the region close to the Lifshitz transition at the topmost moiré valence band, marked by crossing of the van Hove singularity in the density of states. These spin–valley ordered states are dominated by interorbital spin–valley–flips involving the *MM* and *MX* moiré orbitals and occur at different momenta in each side of the van Hove line, indicating a distinct spatial dependence of the spin–valley order parameter depending on the hole filling. Moreover, the corresponding Stoner boundaries exhibit strong fluctuations on its flanks, which can favor superconducting states in the regions close to the spin–valley-ordered ones. This mechanism provides a natural description for a reentrant superconducting dome consistent with the experimental results. As such, our results suggest spin–valley fluctuations near the van-Hove line as the microscopic origin of the reentrant superconductivity in twisted WSe<sub>2</sub>.

## I. INTRODUCTION

The discovery of correlated and superconducting states in moiré materials [1] has opened a new avenue for exploring strongly interacting two-dimensional (2D) systems in a regime where electronic bandwidths, interaction strengths, and topology can all be tuned by design. Since the first observations of correlated insulators and superconductivity in twisted bilayer graphene [2], moiré engineering has emerged as a powerful platform for realizing flat electronic bands with enhanced Coulomb correlations and tunable many-body ground states.

Beyond graphene, transition-metal dichalcogenide (TMD) bilayer systems [3] have recently attracted considerable attention, as they naturally host large spin–orbit coupling, valley-contrasting physics, and strong dielectric confinement, providing a qualitatively distinct route towards correlated and topological quantum phases [4–14].

Among TMD moiré materials, twisted bilayer WSe<sub>2</sub> (tWSe<sub>2</sub>) has recently emerged as a paradigmatic system for correlated electron physics in flat bands. Recent experiments [15–17] have provided compelling evidence for superconductivity in tWSe<sub>2</sub> at twist angles in the 3°–5° range. These superconducting domes typically appear in narrow ranges of carrier density and displacement field, reminiscent of the behavior seen in magic-angle graphene, yet with distinct symmetry and spin properties stemming from the spin–valley–locked nature of TMDs.

While superconducting transitions with critical temperatures of a few hundred millikelvin have been observed near integer fillings of the moiré bands in both cases, at lower twist angles (~3°), superconductivity is found in close proximity to a correlated insulating state [15], resembling the strong-coupling physics of twisted bilayer

graphene. By contrast, at higher twist angles (~5°), superconductivity was found close to a Fermi surface reconstructed magnetic state, which remains metallic [16]. More intriguingly, the experiment at 5° angle [16] found two distinct superconducting regimes: First, along the van Hove singularity and near  $\nu = -1$  electron filling, superconductivity emerges as an isolated superconducting dome. At high electric field, when the density of states becomes even more pronounced, a magnetic state is triggered and splits the superconducting dome in two.

From a theoretical point of view, the superconducting mechanism in tWSe<sub>2</sub> remains subject to intense debate. Theoretical and experimental studies have established that tWSe<sub>2</sub> realizes narrow, isolated moiré bands with strong spin–valley locking and significant Berry curvature. Since the underlying spin–orbit coupling breaks spin degeneracy, the resulting low-energy electronic structure can be viewed as a set of spin–valley polarized bands with effective triangular-lattice geometry, where local Coulomb interactions compete with itinerancy and topological band properties [18–22].

The moiré bands of tWSe<sub>2</sub> can be well described by an effective Hubbard model on a triangular lattice, capturing the interplay between strong on-site and longer-range Coulomb interactions and the geometric frustration inherent to the lattice [18]. Due to the large spin–orbit coupling, the spin and valley degrees of freedom are intertwined, reducing the effective symmetry and allowing for unconventional pairing channels, including mixed singlet–triplet or chiral states [23–25].

Early studies based on mean-field and strong-coupling approaches have found evidence for correlated insulators and possible magnetically mediated superconductivity [26, 27]. In addition, theoretical works have em-

phasized the relevance of van Hove singularities tunable by twist angle or displacement field, which can enhance interaction-driven instabilities in specific momentum channels [10, 28, 29].

A variety of complementary theoretical frameworks have been developed to analyze the interplay of correlations and superconductivity in tWSe<sub>2</sub>. Continuum-model and Wannier-based approaches have clarified the nature of the moiré bands and their evolution with the twist angle, linking small-angle and large-angle regimes through realistic three-band tight-binding models [21, 30]. Strong-coupling and cluster DMFT studies have demonstrated the emergence of  $d+id$ -wave superconductivity in related TMD-based triangular lattices [31], while renormalization-group and variational studies have identified competing spin-singlet, triplet, and pair-density-wave (PDW) instabilities [25, 32–34]. More recent theoretical efforts have focused on the possibility of topological superconductivity emerging from repulsive interactions or from valley-contrasting fluxes [23, 24, 35–37]. Despite this growing theoretical landscape, the microscopic mechanism responsible for pairing and the symmetry of the superconducting order parameter remains unsettled. In addition, several mean-field [26, 30, 38], renormalization group [28, 34], and RPA [39] studies have proposed spin-valley order in tTMDs.

Despite the recent activity in the field, a detailed theoretical explanation for the reentrant superconductivity observed in the  $\sim 5^\circ$  experiments [16] is still absent. In this work, we aim to fill this gap by providing a theoretical study of this topic based on the matrix-RPA (mRPA) method [40, 41]. Within this context, the mRPA framework provides a natural framework to investigate the leading pairing instabilities in tWSe<sub>2</sub> from a weak-to-intermediate coupling perspective, account for pairing vertex diagrams beyond what is usually known as RPA [41, 42]. In fact, one of the main results reported here is that this approach naturally accounts for a signature of reentrant superconductivity resulting from a Stoner-like instability [43] along the van-Hove singular line.

This paper is organized as follows: the three-orbital Wannier-based model for tWSe<sub>2</sub> is discussed in Sec. II while the details of the matrix-RPA calculations are given in Sec. III. The main results for the spin-valley instabilities and the Stoner boundary are given in IV. Our overall conclusions are summarized in Sec. V.

## II. WANNIER-BASED MODEL

### A. Effective Hamiltonian

An effective interacting model for tWSe<sub>2</sub> at a  $5^\circ$  twist angle can be represented by the following Hamiltonian

$$H = H_0 + H_{\text{int}}, \quad (1)$$

where  $H_0$  is the non-interacting term given by the three-orbital model of Refs. [21, 34]

$$H_0 = \sum_{\xi \mathbf{R} \mathbf{R}' pp'} t_{\mathbf{R}p, \mathbf{R}'p'}^\nu c_{\mathbf{R}p\xi}^\dagger c_{\mathbf{R}'p'\xi}, \quad (2)$$

where  $c_{\mathbf{R}p\xi\sigma}^\dagger$  creates an electron with spin-valley  $\xi$ , in the Wannier state  $|\mathbf{R}, p\rangle$  centered at position  $p = \{MM, XM, MX\}$ , as represented in Fig. 1(a), in the unit cell located at the moiré lattice vector  $\mathbf{R}$ . The hopping matrix includes intersublattice and intrasublattice hoppings up to 9 unit-cell distances.

The interacting part of the Hamiltonian,  $H_{\text{int}}$ , is given by [21]

$$H_{\text{int}} = \sum_{\mathbf{R}p\xi} U_p \hat{N}_{\mathbf{R}p\xi} \hat{N}_{\mathbf{R}p(-\xi)}, \quad (3)$$

where  $\hat{N}_{\mathbf{R}p\xi} = c_{\mathbf{R}p\xi}^\dagger c_{\mathbf{R}p\xi}$  is the number operator related to the Wannier state. Here, we consider  $U_{XM} = U_{MX} \approx 41.3$  meV and  $U_{MM}/U_{XM} \approx 0.90$  as to reproduce the onset of superconductivity near  $\nu = -1$  as in the experiments, which here happens for electric fields  $E_z \sim 20$  meV.

### B. Density of states: van Hove singularity and Lifshitz transition

Let us first review the main features of the non-interacting band structure given by diagonalizing  $H_0$  (Eq. (2)). As shown in Fig. 1(a), the three orbitals represent a triangular ( $MM$  orbital) and hexagonal ( $XM$  and  $MX$  orbitals) lattices. Also, since the strong spin-orbit coupling in each WSe<sub>2</sub> monolayer induces spin-valley locking [19], spin and valley quantum numbers are denoted by a single spin-valley index  $\xi = \{(\uparrow +), (\downarrow -)\}$ . Time-reversal symmetry (momentum inversion plus  $\xi \rightarrow -\xi$ ) ensures that  $H_0$  block-diagonal in the spin-valley index  $\xi$ .

The three-orbital construction of Ref. [34] takes into account the topological properties of the low-lying hole bands in the continuum model, providing an overall zero net Chern number, thus allowing for a Wannier obstruction-free, faithful description of the band structure. We show a representative band structure in Fig. 1(b) for electric field  $E_z = 20$  meV and electron filling  $\nu = -1$ . Here, the filling factor is defined by normalizing the three-band total occupation  $n$  to 6 electrons in total, three for each spin-valley such that  $\nu = n - 6$ . The topmost band will be the hole-doping band, which is experimentally accessible and hosts up to two holes ( $\nu = -2$ ).

In Fig. 2(a) we show a color map of the electron density of states as a function of the displacement field  $E_z$  and the electron filling factor  $\nu$ , which can be directly compared with the resistance maps in the  $\sim 5^\circ$  twist angle experiment [16]. A darker green color marks the van Hove singularity.

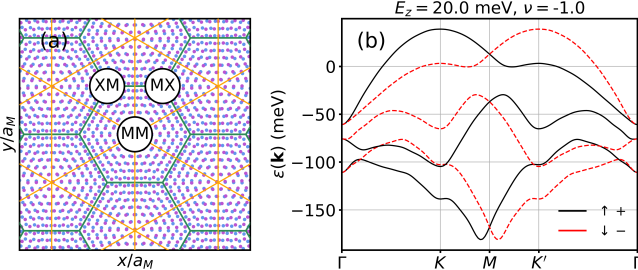


FIG. 1. Schematic of the non-interacting model we used, obtained by Wannierizing the tTMDh continuum model [21]. Panel (a) shows a depiction of the real-space moiré superlattice for  $\theta = 5^\circ$  centered at an  $MM$  sublattice site. This model considers two lattices, a triangular lattice of  $MM$  sites (yellow lines), and a hexagonal lattice of  $MX$  and  $XM$  sites (green lines). Intralattice and interlattice hoppings are taken into account for distances up to 9 unit cells. In panel (b), we show a representative band structure of the three-orbital model for electron filling  $\nu = -1$  and electric field  $E_z = 20$  meV.

In order to properly compare our results to the experimental phase diagram, we notice that Ref. [16] reports superconductivity near the van Hove singularity at  $\nu = -1$ . This restricts the relevant electric field regions to about  $E_z \sim 20$  meV. Fig. 2(b) shows (from top to bottom) the Fermi surfaces at constant  $E_z = 20$  meV and filling factors  $\nu = -1.1, -1.05, -0.95$ , respectively marked by circle (yellow), square (green) and diamond (purple) symbols in panel (a). This sequence nicely illustrates the Lifshitz transition marked by the appearance of a small hole pocket at  $K'$  and the subsequent crossing of the van Hove singularity (VHS), leading to a sharp increase in the density of states [38].

### III. SPIN-VALLEY FLUCTUATIONS: MATRIX-RPA FORMALISM

In the following, we describe the matrix RPA steps used in our analysis.

Our goal is to probe the instabilities caused by spin-valley quantum fluctuations. By incorporating the spin and charge fluctuations arising from Coulomb interactions on the moiré lattice, the mRPA approach allows one to identify the dominant momentum-dependent pairing channels and to distinguish between competing spin-singlet and spin-triplet superconducting states.

The spin-valley-locked band structure of tWSe<sub>2</sub> introduces additional complexity, as spin and momentum are no longer independent quantum numbers. Consequently, the effective interaction vertices acquire a pronounced dependence on valley and orbital composition, which can qualitatively modify the competition between even- and odd-parity pairing. This formalism has been successfully applied in related 2D systems to describe nematic, chi-

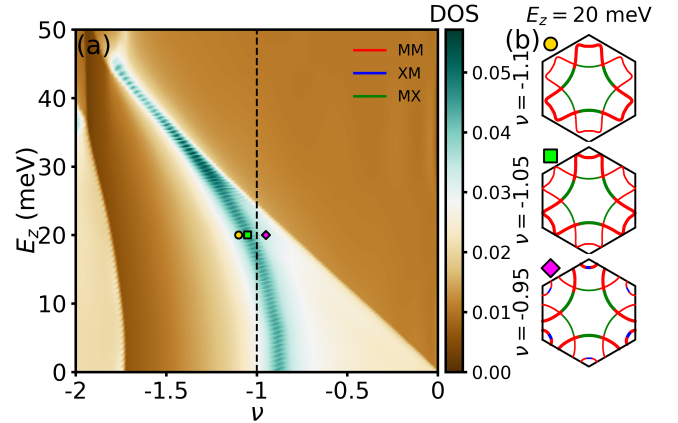


FIG. 2. Panel (a) shows a color map of the density of states in an electric field  $E_z$  by electron filling  $\nu$  diagram. A black vertical dashed line marks the  $\nu = -1$  filling, which is relevant for the experimental phase diagram. The dark green region of the phase diagram marks the van Hove singularity (VHS). The yellow circle, green square and purple diamond symbols marks points of the phase diagram at constant electric field  $E_z = 20$  meV for which we show Fermi surfaces in panel (b). From top to bottom, panel (b) shows a Lifshitz transition and the crossing of the VHS by the Fermi energy, marked by a steep increase in the DOS. Orbital contributions to the Fermi surfaces are shown in colors, i.e. red for  $MM$ , blue for  $XM$  and green for  $MX$ . Spin-valleys ( $\uparrow +$ ) and ( $\downarrow -$ ) are represented by thicker and thinner lines, respectively.

ral, and topological superconductivity mediated by spin fluctuations [38, 39]. In the context of moiré TMDs, however, a fully microscopic RPA treatment that explicitly includes spin-valley locking, realistic band dispersions, and interlayer coupling has not yet been comprehensively explored.

The starting point is the bare (non-interacting) static multi-orbital susceptibility matrix elements [40, 43–45] relating orbital ( $p, q, r, t$ ) and spin-valley ( $\xi, \xi'$ ) indices as:

$$[\chi_0(\mathbf{q})]_{r\xi, t\xi'}^{p\xi', q\xi} = -\frac{T}{N_{\mathbf{k}}} \sum_{\mathbf{k} i\omega_n} G_{t\xi p\xi}(\mathbf{k}, i\omega_n) \times G_{q\xi' r\xi'}(\mathbf{k} + \mathbf{q}, i\omega_n), \quad (4)$$

where

$$G_{t\xi p\xi}(\mathbf{k}, i\omega_n) = \sum_{\nu\nu'} \frac{\psi_{\nu}^{t\xi}(\mathbf{k}) \psi_{\nu'}^{p\xi*}(\mathbf{k})}{E_{\nu}^{\xi}(\mathbf{k}) - E_{\nu'}^{\xi'}(\mathbf{k})} \quad (5)$$

which depend on the eigenvalues  $E_{\nu}^{\xi}(\mathbf{k})$  of the non-interacting Hamiltonian  $H_0$  [Eq. (2)], and on the eigenvector coefficients  $\psi_{\nu}^{p\xi}(\mathbf{k}) \equiv \langle p|\nu\mathbf{k}\rangle_{\xi}$ , which correspond to the projection of band state  $|\nu\mathbf{k}\rangle_{\xi}$  into the Wannier orbital  $|p\rangle_{\xi}$  at valley  $\xi$ .

In our model with 3 Wannier orbitals per spin-valley,  $\hat{\chi}_0(\mathbf{q})$  is a  $36 \times 36$  matrix spanning the  $\{p\xi', q\xi\}$  basis.

In Eq. (4),  $N_{\mathbf{k}}$  is the number of Brillouin zone  $\mathbf{k}$ -points considered in the summation, and  $T$  is the temperature. Throughout this work, we used a summation grid of  $256 \times 256$   $\mathbf{k}$ -points in the triangular lattice Brillouin zone, up to  $\pm 300$  meV imaginary frequencies using the discrete Lehmann representation [44–46] at a temperature  $T = 0.03$  meV = 352 mK.

We write the RPA spin-valley susceptibility suitable for detecting magnetism and valley order in the system as [40, 47]

$$\hat{\chi}(\mathbf{q}) = \hat{\chi}_0(\mathbf{q}) \left[ \hat{1} - \hat{U}(\mathbf{q}) \hat{\chi}_0(\mathbf{q}) \right]^{-1}, \quad (6)$$

where the non-zero  $\hat{U}$  matrix elements can be written in terms of the  $U_p$  defined in Eq. (3) as:

$$[U]_{p\xi, p\xi'}^{p\xi, p\xi'} = U_p \delta_{\xi\xi'}. \quad (7)$$

The generalized Stoner criterion (namely, the vanishing of the denominator in Eq. (6)) establishes the condition for the transition between a paramagnetic (uniform density) state possibly favoring the SC phase, and a spin-valley ordered one, which necessarily suppresses superconductivity. We define the spin-valley ( $\alpha$ ) critical Stoner parameter by solving the following eigenvalue equations [48]

$$\det \left( \hat{1}\alpha - \hat{U}\hat{\chi}_0 \right) = 0. \quad (8)$$

Defining the main Stoner parameter  $\max\{\alpha\} \equiv \alpha_c$ , the Stoner criterion is fulfilled when  $\alpha_c = 1$ . Notice that  $\alpha_c > 1$  indicates spin-valley ordering for any nonzero value of the interaction  $U_p$ , thus completely suppressing superconductivity. As such, we define the line in parameter space marked by  $\alpha_c = 1$  as the *Stoner boundary* [43].

In this sense, the diverging components of the RPA spin-valley susceptibility matrix  $\hat{\chi}(\mathbf{q})$  (Eq. (6)) at  $\mathbf{q} = \mathbf{Q}$  and at a critical parameter can be associated with a spin-valley phase transition and the emergence of an order parameter  $\Delta(\mathbf{Q})$  with ordering vector  $\mathbf{Q}$ .

In fact, as discussed in Refs. [49, 50], information on the order parameter at the instability point ( $\alpha_c = 1$ ) can be obtained from the eigenvector  $\Delta_{p\xi t\xi'}$  associated with the leading eigenvalue  $\chi^{\text{eig}}(\mathbf{q})$  of  $\hat{\chi}(\mathbf{q})$ :

$$\sum_{r\xi, q\xi'} [\hat{\chi}(\mathbf{q})]_{r\xi, q\xi'}^{p\xi t\xi'} \Delta_{r\xi q\xi'} = \chi^{\text{eig}}(\mathbf{q}) \Delta_{p\xi t\xi'} \quad (9)$$

By finding the vector  $\mathbf{Q}$  at which  $\chi^{\text{eig}}(\mathbf{q} = \mathbf{Q})$  diverges for  $\alpha_c = 1$ , the order parameter can then be written as [49]

$$\Delta(\mathbf{Q}) \propto \sum_{p\xi t\xi'} \Delta_{p\xi t\xi'} \langle S_{p\xi s\xi'}(\mathbf{Q}) \rangle, \quad (10)$$

where

$$S_{p\xi s\xi'}(\mathbf{Q}) = \sum_{\mathbf{k}} c_{(\mathbf{k}+\mathbf{Q})p\xi}^{\dagger} (\boldsymbol{\sigma})_{\xi\xi'} c_{\mathbf{k}t\xi'}. \quad (11)$$

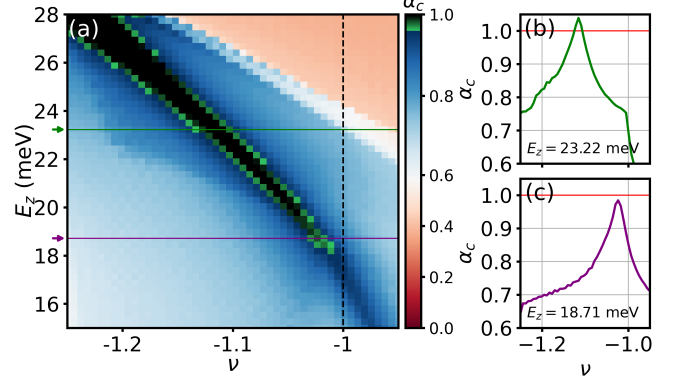


FIG. 3. Stoner phase diagram. Panel (a) shows the critical Stoner parameter  $\alpha_c$  in the electric field  $E_z$  by electron filling  $\nu$  diagram at Hubbard interaction  $U_{XM} = U_{MX} \approx 41.3$  meV and  $U_{MM}/U_{XM} \approx 0.90$ . The green color interpolates with black for  $0.95 \leq \alpha_c \leq 1$  and the black colors characterize  $\alpha_c \geq 1$ .  $\alpha_c \geq 1$  means the Stoner criterion, marking the ordered state, has been achieved. Panels (b) and (c) shows constant electric field cuts for  $E_z = 23.22$  meV (green) and  $E_z = 18.71$  meV (purple) of the phase diagram. The constant  $\alpha_c = 1$  red line marks the Stoner boundary.

is the spin operator and  $\boldsymbol{\sigma}$  is the Pauli vector. Thus, we can obtain information on the order parameter  $\Delta(\mathbf{Q})$  by numerically evaluating Eq. (9) near/at the Stoner boundary.

#### IV. SUPERCONDUCTIVITY VS. SPIN-VALLEY ORDER

We now turn to the phase diagram based on the Stoner criteria for spin-valley fluctuations, showing the boundary marking the spin-valley ordered phase.

##### A. Stoner boundary

Fig. 3(a) shows the critical Stoner parameter  $\alpha_c$  in a colormap as a function of the displacement field  $E_z$  and electron filling  $\nu$ . The green to black gradient marks the  $0.95 \leq \alpha_c \leq 1$  region. Black color denotes  $\alpha_c \geq 1$ , defining the spin-valley ordered region.

At  $E_z \approx 20$  meV, there is spin-valley order along the van Hove singularity line (black color), and high  $\alpha_c$  regions at the flanks of the ordered state. Fig. 3(b) shows an  $E_z = 23.07$  meV cut [green arrow in panel (a)], where we remark the ordered region ( $\alpha_c > 1$ ). When  $E_z \approx 18$  meV, there is no spin-valley order, but the critical Stoner parameter is still very high, as depicted in panel (c) [purple arrow in panel (a)].

The results shown in Fig. 3 are consistent with the reentrant superconducting state as observed in the experiments [16] and constitute one of the main results of

this paper. Since the superconducting phase is favored near the instability line, where the pairing is stronger and the SC order parameter tends to be larger [40, 43], the green-black-green color pattern shows that the system can go from a superconducting-ordered state (green) to a spin-valley ordered state (black) by varying the electron filling in the region  $20 \lesssim E_z \lesssim 21$  meV shown in Fig. 3(a), thus characterizing a reentrant superconducting state similar to that seen in the experimental results of Ref. [16]. We remark that to the best of our knowledge, no other model has predicted this reentrant behavior in the range of parameters consistent with the experimental ones.

## B. Spin-valley order and reentrant superconductivity

In order to obtain the spin-valley order parameter  $\Delta(\mathbf{Q})$  (Eq. (10)), we numerically solve Eq. (9) near the  $\alpha_c = 1$  transition lines in the phase diagram shown in Fig. 3, to determine the leading eigenvalues  $\chi^{\text{eig}}(\mathbf{q})$  of the susceptibility matrix, as well as the divergent nesting vectors  $\mathbf{Q}$ . These results are shown in Fig. 4, where we show  $\chi^{\text{eig}}(\mathbf{q})$  close to the Stoner boundary (we set  $U = 0.99U_c$ ) for  $E_z = 20$  meV and fillings  $\nu$  corresponding to the colored markers shown in Fig. 2(a).

For  $\nu = -1.05$ , corresponding to the van Hove line in the DOS,  $\chi^{\text{eig}}(\mathbf{q})$  diverges at  $\mathbf{Q} \equiv \mathbf{Q}_1 = 0$ . In fact, the  $\mathbf{Q} = 0$  divergence persists for the *entire* van Hove line in the phase diagram. This result can be understood as follows: at  $\mathbf{q} = 0$  and  $T = 0$ , the homogeneous non-interacting susceptibility is proportional to the density of states at the Fermi level [40]. As such, a divergence in the density of states (such as a van Hove singularity associated with a Lifshitz transition) will manifest itself as a  $\mathbf{Q} = 0$  divergence both in the homogeneous and interacting susceptibilities.

Given the results for  $\chi^{\text{eig}}(\mathbf{q})$  and the corresponding eigenvectors at the Stoner boundary, the leading contributions to the spin-valley order parameter can be obtained from Eq. (10). For  $\nu = -1.05$ , we find that the leading eigenvector components are  $\Delta_{(MM\uparrow)(MM\uparrow)} = -\Delta_{(MX\downarrow)(MX\downarrow)}$ . Thus, our results are consistent with a spin-valley order parameter of the form

$$\Delta_z(\mathbf{Q} \approx \mathbf{0}) \propto \Delta \left[ \sum_{\mathbf{k}} \langle c_{(\mathbf{k})(MM\uparrow)}^\dagger c_{\mathbf{k}(MM\uparrow)} \rangle + \langle c_{(\mathbf{k})(MX\downarrow)}^\dagger c_{\mathbf{k}(MX\downarrow)} \rangle \right], \quad (12)$$

where we have defined  $\Delta \equiv \Delta_{(MM\uparrow)(MM\uparrow)}$ .

Therefore, considering the electron concentration in the  $MM$  and  $XM$  orbitals, our mRPA results are consistent with a commensurate spin-valley ordered phase with  $MM - MM$  and  $XM - XM$  ferromagnetic alignment, as well as a  $MM - MX$  antiferromagnetic alignment, as depicted in the inset of Fig. 4.

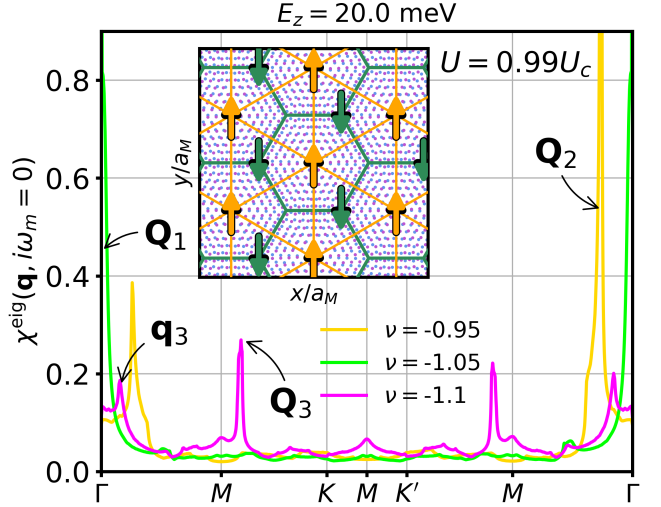


FIG. 4. Main eigenvalue of the spin-valley susceptibilities along the Brillouin zone high-symmetry directions. Line colors correspond to the same points in the phase diagram as the symbols in Fig. 2(a). For each curve, we set the main Hubbard interaction,  $U_{MX}$ , to be  $0.99U_c$ , where  $U_c$  is the critical Hubbard interaction to trigger the Stoner criterion. The inset shows the homogeneous spin-valley susceptibility matrix elements for  $[\chi(\mathbf{q})]_{p\xi,p\xi}^*$  at the van Hove singularity filling  $\nu = -1.05$ .

For filling factors slightly larger than the van Hove value (e.g.,  $\nu = -0.95$ , purple curve in Fig. 4), the divergence still occurs at  $\mathbf{Q}_2 \approx 0$ , indicating the same type of magnetic order. Now, for fillings slightly lower than the van Hove value (e.g.,  $\nu = -1.1$ , yellow curve in Fig. 4), the divergence occurs for  $\mathbf{Q}_3 \approx (\pi, 0)$ , near the  $M$  point. In this case, the order parameter is of the form

$$\Delta_z(\mathbf{Q} \approx \mathbf{Q}_3) \propto \Delta \sum_{\mathbf{k}} \langle c_{(\mathbf{k}+\mathbf{Q}_3)(MM\uparrow)}^\dagger c_{\mathbf{k}(MM\uparrow)} \rangle, \quad (13)$$

Notice, however, that the sharp peak in  $\chi^{\text{eig}}(\mathbf{q})$  at  $\mathbf{q} = \mathbf{q}_3 \approx 0$  for  $\nu = -1.1$  indicates that the zero-momentum contribution to spin scattering is still very strong, even for values of  $U$  very close to the transition value ( $U = 0.99U_c$ ). This supports a picture in which spin-fluctuations favor superconductivity in this side of the van Hove line as well.

These results can also give insights on the reentrant superconductivity observed experimentally. In fact, while superconductivity is suppressed in the spin-valley ordered regions of the phase diagram, it tends to be highly favored in the regions located at the paramagnetic flanks of the Stoner boundary (green regions of Fig. 3(a)), especially since the peaks at  $\chi^{\text{eig}}(\mathbf{q} = 0)$  for fillings in this region will play the dominant contribution to the pairing interaction [40].

The strengthening of superconductivity at the edges of the Stoner boundary can be understood by taking the single-orbital Hubbard model as an example. In this

case, Eq. (8) is algebraic and the Stoner criterion at zero temperature is expressed by  $\alpha = \chi_0(0)U \propto \rho_0 U$ , where  $\rho_0$  is the density of states at the Fermi energy and  $U$  is the Hubbard interaction strength. On the other hand, a BCS superconductor has a critical temperature  $T_c \sim e^{-1/\lambda}$  with  $\lambda = \rho_0 V$  the pairing strength for a system with Fermi surface density of states  $\rho_0$  and effective electron-electron interaction  $V$ . At this simplified level,  $U$  and  $V$  are constants and we notice the similarity between  $\alpha$  and  $\lambda$ : The density of states. When the density of states is high enough,  $\alpha > 1$  and the spin-valley order sets in. However, when  $\alpha \lesssim 1$ ,  $\lambda \sim \alpha V/U$  favors the superconducting pairing. In this way, we expect the green region in Fig. 3(a) to be superconducting. These arguments have been considered quantitatively at the mean-field level [51].

## V. CONCLUDING REMARKS

In this work, we have investigated the interplay between spin-valley instabilities and superconductivity in twisted bilayer WSe<sub>2</sub> at a twist angle of 5°, motivated by recent experimental observations of reentrant superconducting behavior. Starting from a faithful three-orbital Wannier description of the spin-valley-locked moiré bands and incorporating orbital-dependent Hubbard interactions, we employed a matrix random phase approximation (mRPA) framework to analyze the evolution of magnetic instabilities as a function of hole filling and perpendicular electric field.

By computing the spin-valley susceptibilities across the electric-field-density phase diagram, we identified the Stoner boundary lines associated with the onset of spin-valley ordered states. These instabilities occur in close proximity to a Lifshitz transition in the topmost moiré valence band, marked by the crossing of a van Hove singularity in the density of states. The Lifshitz transition separates regimes with distinct Fermi-surface topologies, and its presence strongly enhances spin-valley fluctuations, providing favorable conditions for interaction-driven ordering phenomena.

Our analysis reveals that the dominant spin-valley instabilities are governed by interorbital spin-valley-flip processes involving the *MM* and *MX* moiré orbitals. Importantly, the momentum structure of the leading instability changes across the van Hove line, indicating that the spatial pattern of the spin-valley order parameter depends sensitively on carrier density. This filling-dependent momentum selection highlights the crucial role played by the multi-orbital character of the moiré bands and the underlying Lifshitz transition in shaping the nature of the ordered states.

Beyond the emergence of spin-valley order, we find that the Stoner boundary lines are accompanied by pronounced fluctuations on their flanks. Within the mRPA framework, these enhanced spin-valley fluctuations naturally give rise to attractive pairing interactions in nearby

regions of the phase diagram. As a result, superconducting instabilities are favored in the vicinity of, but not inside, the spin-valley-ordered phases. This mechanism provides a microscopic explanation for a reentrant superconducting dome surrounding magnetically ordered regions, in qualitative agreement with experimental observations in twisted bilayer WSe<sub>2</sub> at 5°.

More broadly, our results underscore the central role of Fermi-surface topology and multi-orbital spin-valley physics in moiré transition-metal dichalcogenides. The close connection between a Lifshitz transition, enhanced spin-valley fluctuations, and reentrant superconductivity identified here suggests a unifying framework for understanding correlated and superconducting phases in twisted WSe<sub>2</sub> and related systems. Future work incorporating self-energy effects beyond mRPA, as well as a more explicit treatment of superconducting pairing channels, may further clarify the symmetry and robustness of the superconducting states and their interplay with competing orders.

## ACKNOWLEDGMENTS

We thank George G. Martins for insightful discussions on the mRPA method. LBB thanks Valentin Crépel for presenting the open problem of reentrant superconductivity in ~5° twisted bilayer WSe<sub>2</sub>, and Hugo Strand and Andrew Hardy for personalized implementations of the general susceptibility within TRIQS TPRF. We acknowledge financial support by CNPq (309789/2020-6, and 312622/2023-6), and FAPESP (grant Nos. 2022/15453-0, 2023/14902-8, and 2025/17852-7).

## Appendix A: Efficient computation of the spin-valley susceptibility

Computing the susceptibility of a multiorbital system is a formidable problem. The susceptibility is defined in the two-body basis formed by one electron that can tunnel from spin-valley orbital  $t\xi_4$  to  $p\xi_1$  which scatters with another electron tunneling from  $q\xi_2$  to  $r\xi_3$ .

With  $N_\xi$  spin-valley indices and  $N_o$  orbitals, this basis has dimension  $N_\xi^2 N_o^2$ , which in the susceptibility translates to a matrix with  $N_\xi^4 N_o^4$  elements. For each of these elements, the momentum and imaginary frequency summations of Eq. (4) must be performed. With  $N_\mathbf{k}$   $\mathbf{k}$  points and  $N_\omega$  imaginary frequencies, using Fourier transformations makes the problem simpler, and computations grow with  $N_\xi^4 N_o^4 N_\mathbf{k} N_\omega \ln(N_\mathbf{k} N_\omega)$  complexity [46] as implemented in the TPRF package [45] of the TRIQS library [44]. This is in contrast with the analytical expression for the susceptibility which requires  $N_\xi^4 N_o^4 N_\mathbf{k}^2$  operations [40]. Here,  $N_o = 3$  and  $N_\xi = 2$ , so, in principle, 1296 summations should be performed. However, there is one aspect of the non-interacting model

that helps in this task: The two spin-valleys are decoupled in the non-interacting Hamiltonian  $H_0$ . With this in mind, we note that the only non-zero matrix elements of the bare susceptibility are those such that  $\xi_1 = \xi_4$  and  $\xi_2 = \xi_3$  for which the Green's functions of Eq. (4) keep only intra-spin-valley terms. Omitting the orbital indices for conciseness, we only need to compute the susceptibility elements  $[\chi_0(\mathbf{q}, 0)]_{\uparrow, \uparrow}^{\uparrow, \uparrow}$ ,  $[\chi_0(\mathbf{q}, 0)]_{\downarrow, \downarrow}^{\downarrow, \downarrow}$ ,  $[\chi_0(\mathbf{q}, 0)]_{\uparrow, \downarrow}^{\downarrow, \uparrow}$ , and  $[\chi_0(\mathbf{q}, 0)]_{\downarrow, \uparrow}^{\uparrow, \downarrow}$  in the three-orbital space ( $N_o = 3$ ). Thus, instead of one  $N_o N_\xi = 6$  problem, we end up with four  $N_o = 3$  problems, which lowers the number of matrix elements computed from 1296 to 324.

---

[1] E. Y. Andrei, D. K. Efetov, P. Jarillo-Herrero, A. H. MacDonald, K. F. Mak, T. Senthil, E. Tutuc, A. Yazdani, and A. F. Young, The marvels of moiré materials, *Nat. Rev. Mat.* **6**, 201 (2021).

[2] Y. Cao, V. Fatemi, S. Fang, K. Watanabe, T. Taniguchi, E. Kaxiras, and P. Jarillo-Herrero, Unconventional superconductivity in magic-angle graphene superlattices, *Nature* **556**, 43.

[3] B. Li, W.-X. Qiu, F. Wu, and A. H. MacDonald, Quantum phases in twisted homobilayer transition metal dichalcogenides (2025), arXiv:2509.07360 [cond-mat.str-el].

[4] L. Wang, E.-M. Shih, A. Ghiotto, L. Xian, D. A. Rhodes, C. Tan, M. Claassen, Y. Kennes, Dante M. and Bai, B. Kim, K. Watanabe, T. Taniguchi, X. Zhu, J. Hone, A. Rubio, A. N. Pasupathy, and C. R. Dean, Correlated electronic phases in twisted bilayer transition metal dichalcogenides, *Nat. Mat.* **19**, 861 (2020).

[5] Y. Xu, K. Kang, K. Watanabe, T. Taniguchi, K. F. Mak, and J. Shan, A tunable bilayer hubbard model in twisted WSe<sub>2</sub>, *Nat. Nanotechnol.* **17**, 934 (2022).

[6] E. Anderson, F.-R. Fan, J. Cai, W. Holtzmann, T. Taniguchi, K. Watanabe, D. Xiao, W. Yao, and X. Xu, Programming correlated magnetic states with gate-controlled moiré geometry, *Science* **381**, 325 (2023).

[7] J. Cai, E. Anderson, C. Wang, X. Zhang, X. Liu, W. Holtzmann, Y. Zhang, F. Fan, T. Taniguchi, K. Watanabe, Y. Ran, T. Cao, L. Fu, D. Xiao, W. Yao, and X. Xu, Signatures of fractional quantum anomalous hall states in twisted MoTe<sub>2</sub>, *Nature* **622**, 63 (2023).

[8] Y. Zeng, Z. Xia, K. Kang, J. Zhu, P. Knüppel, C. Vaswani, K. Watanabe, T. Taniguchi, K. F. Mak, and J. Shan, Thermodynamic evidence of fractional chern insulator in moiré MoTe<sub>2</sub>, *Nature* **622**, 69 (2023).

[9] H. Park, J. Cai, E. Anderson, Y. Zhang, J. Zhu, X. Liu, C. Wang, W. Holtzmann, C. Hu, Z. Liu, T. Taniguchi, K. Watanabe, J.-H. Chu, T. Cao, L. Fu, W. Yao, C.-Z. Chang, D. Cobden, D. Xiao, and X. Xu, Observation of fractionally quantized anomalous hall effect, *Nature* **622**, 74 (2023).

[10] B. A. Foutty, C. R. Kometter, T. Devakul, A. P. Reddy, K. Watanabe, T. Taniguchi, L. Fu, and B. E. Feldman, Mapping twist-tuned multiband topology in bilayer WSe<sub>2</sub>, *Science* **384**, 343 (2024).

[11] F. Xu, Z. Sun, T. Jia, C. Liu, C. Xu, C. Li, Y. Gu, K. Watanabe, T. Taniguchi, B. Tong, J. Jia, Z. Shi, S. Jiang, Y. Zhang, X. Liu, and T. Li, Observation of integer and fractional quantum anomalous hall effects in twisted bilayer MoTe<sub>2</sub>, *Phys. Rev. X* **13**, 031037 (2023).

[12] A. Ghiotto, L. Wei, L. Song, J. Zang, A. B. Tazi, D. Ostrom, K. Watanabe, T. Taniguchi, J. C. Hone, D. A. Rhodes, A. J. Millis, C. R. Dean, L. Wang, and A. N. Pasupathy, Stoner instabilities and ising excitonic states in twisted transition metal dichalcogenides (2024), arXiv:2405.17316 [cond-mat.str-el].

[13] A. Ghiotto, E.-M. Shih, G. S. S. G. Pereira, D. A. Rhodes, B. Kim, J. Zang, A. J. Millis, K. Watanabe, T. Taniguchi, J. C. Hone, L. Wang, C. R. Dean, and A. N. Pasupathy, Quantum criticality in twisted transition metal dichalcogenides, *Nature* **597**, 345 (2021).

[14] T. G. Kiely and D. Chowdhury, Continuous wigner-mott transitions at  $\nu = 1/5$ , *Phys. Rev. B* **110**, L241112 (2024).

[15] Y. Xia, Z. Han, K. Watanabe, T. Taniguchi, J. Shan, and K. F. Mak, Superconductivity in twisted bilayer WSe<sub>2</sub>, *Nature* **637**, 833 (2025).

[16] Y. Guo, J. Pack, J. Swann, L. Holtzman, M. Cothrine, K. Watanabe, T. Taniguchi, D. G. Mandrus, K. Barmak, J. Hone, A. J. Millis, A. Pasupathy, and C. R. Dean, Superconductivity in 5.0° twisted bilayer WSe<sub>2</sub>, *Nature* **637**, 839 (2025).

[17] P. Knüppel, J. Zhu, Y. Xia, Z. Han, Y. Zeng, K. Watanabe, T. Taniguchi, J. Shan, and K. F. Mak, Correlated states controlled by tunable van hove singularity in moiré WSe<sub>2</sub> (2024).

[18] H. Pan, F. Wu, and S. Das Sarma, Band topology, hubbard model, heisenberg model, and dzyaloshinskii-moriya interaction in twisted bilayer WSe<sub>2</sub>, *Phys. Rev. Res.* **2**, 033087 (2020).

[19] A. Kormányos, G. Burkard, M. Gmitra, J. Fabian, V. Zólyomi, N. D. Drummond, and V. Fal'ko,  $\mathbf{k} \cdot \mathbf{p}$  theory for two-dimensional transition metal dichalcogenide semiconductors, *2D Materials* **2**, 022001 (2015).

[20] T. Devakul, V. Crépel, Y. Zhang, and L. Fu, Magic in twisted transition metal dichalcogenide bilayers, *Nat. Comm.* **12**, 6730 (2021).

[21] V. Crépel and A. Millis, Bridging the small and large in twisted transition metal dichalcogenide homobilayers: A tight-binding model capturing orbital interference and topology across a wide range of twist angles, *Phys. Rev. Res.* **6**, 033127 (2024).

[22] Y. Zhang, H. Pi, J. Liu, W. Miao, Z. Qi, N. Regnault, H. Weng, X. Dai, B. A. Bernevig, Q. Wu, and J. Yu, Universal moiré-model-building method without fitting: Application to twisted MoTe<sub>2</sub> and WSe<sub>2</sub> (2024), arXiv:2411.08108 [cond-mat.mes-hall].

[23] W. Akbar, A. Biborski, L. Rademaker, and M. Zegrodnik, Topological superconductivity with mixed singlet-triplet pairing in moiré transition metal dichalcogenide bilayers, *Phys. Rev. B* **110**, 064516 (2024).

[24] M. Zegrodnik and A. Biborski, Mixed singlet-triplet superconducting state within the moiré model applied to twisted bilayer, *Phys. Rev. B* **108**, 064506 (2023).

[25] Y.-M. Wu, Z. Wu, and H. Yao, Pair-density-wave and chi-

ral superconductivity in twisted bilayer transition metal dichalcogenides, *Phys. Rev. Lett.* **130**, 126001 (2023).

[26] S. Kim, J. F. Mendez-Valderrama, X. Wang, and D. Chowdhury, Theory of correlated insulators and superconductor at  $\nu = 1$  in twisted WSe<sub>2</sub>, *Nat. Comm.* **16**, 1701 (2025).

[27] A. Abouelkomsan, E. J. Bergholtz, and S. Chatterjee, Multiferroicity and topology in twisted transition metal dichalcogenides, *Phys. Rev. Lett.* **133**, 026801 (2024).

[28] Y.-T. Hsu, F. Wu, and S. Das Sarma, Spin-valley locked instabilities in moiré transition metal dichalcogenides with conventional and higher-order van hove singularities, *Phys. Rev. B* **104**, 195134 (2021).

[29] J. Zhu, Y.-Z. Chou, M. Xie, and S. Das Sarma, Superconductivity in twisted transition metal dichalcogenide homobilayers, *Phys. Rev. B* **111**, L060501 (2025).

[30] V. Crépel and A. Millis, Spinon pairing induced by chiral in-plane exchange and the stabilization of odd-spin chern number spin liquid in twisted mote<sub>2</sub>, *Phys. Rev. Lett.* **133**, 146503 (2024).

[31] M. Bélanger, J. Fournier, and D. Sénechal, Superconductivity in the twisted bilayer transition-metal dichalcogenide: A quantum cluster study, *Phys. Rev. B* **106**, 235135 (2022).

[32] F. Chen and D. N. Sheng, Singlet, triplet, and pair density wave superconductivity in the doped triangular-lattice moiré system, *Phys. Rev. B* **108**, L201110 (2023).

[33] B. Zhou and Y.-H. Zhang, Chiral and nodal superconductors in the  $t - J$  model with valley contrasting flux on a triangular moiré lattice, *Phys. Rev. B* **108**, 155111 (2023).

[34] A. Fischer, L. Klebl, V. Crépel, S. Ryee, A. Rubio, L. Xian, T. O. Wehling, A. Georges, D. M. Kennes, and A. J. Millis, Theory of intervalley-coherent afm order and topological superconductivity in tWSe<sub>2</sub> (2024), arXiv:2412.14296 [cond-mat.str-el].

[35] C. Tuo, M.-R. Li, Z. Wu, W. Sun, and H. Yao, Theory of topological superconductivity and antiferromagnetic correlated insulators in twisted bilayer WSe<sub>2</sub>, *Nat. Comm.* **16**, 9525 (2025).

[36] D. Guerci, D. Kaplan, J. Ingham, J. H. Pixley, and A. J. Millis, Topological superconductivity from repulsive interactions in twisted wse<sub>2</sub> (2024), arXiv:2408.16075 [cond-mat.supr-con].

[37] Y.-M. Xie and K. T. Law, Orbital fulde-ferrell pairing state in moiré ising superconductors, *Phys. Rev. Lett.* **131**, 016001 (2023).

[38] D. Muñoz Segovia, V. Crépel, R. Queiroz, and A. J. Milis, Twist-angle evolution of the intervalley-coherent antiferromagnet in twisted wse<sub>2</sub>, *Phys. Rev. B* **112**, 085111 (2025).

[39] C. Schrade and L. Fu, Nematic, chiral, and topological superconductivity in twisted transition-metal dichalcogenides, *Phys. Rev. B* **110**, 035143 (2024).

[40] S. Graser, T. A. Maier, P. J. Hirschfeld, and D. J. ino, Near-degeneracy of several pairing channels in multiorbital models for the Fe pnictides, *New J. Phys.* **11**, 025016 (2009).

[41] M. Altmeyer, D. Guterding, P. J. Hirschfeld, T. A. Maier, R. Valentí, and D. J. Scalapino, Role of vertex corrections in the matrix formulation of the random phase approximation for the multiorbital Hubbard model, *Phys. Rev. B* **94**, 214515 (2016).

[42] G. Esirgen, H.-B. Schüttler, and N. E. Bickers, *d*-Wave Pairing in the Presence of Long-Range Coulomb Interactions, *Phys. Rev. Lett.* **82**, 1217 (1999).

[43] L. B. Braz, G. B. Martins, and L. G. G. V. Dias da Silva, Superconductivity from spin fluctuations and long-range interactions in magic-angle twisted bilayer graphene, *Phys. Rev. B* **109**, 184502 (2024).

[44] O. Parcollet, M. Ferrero, T. Ayral, H. Hafermann, I. Krivenko, L. Messio, and P. Seth, Triqs: A toolbox for research on interacting quantum systems, *Comp. Phys. Comm.* **196**, 398–415 (2015).

[45] H. U. R. Strand, Two-particle response function toolbox (tprf) for triqs, <https://github.com/TRIQS/tprf> (2019), GitHub repository.

[46] J. Kaye, K. Chen, and O. Parcollet, Discrete lehmann representation of imaginary-time green's functions, *Phys. Rev. B* **105**, 235115 (2022).

[47] A. T. Rømer, D. D. Scherer, I. M. Eremin, P. J. Hirschfeld, and B. M. Andersen, Knight shift and leading superconducting instability from spin fluctuations in Sr<sub>2</sub>RuO<sub>4</sub>, *Phys. Rev. Lett.* **123**, 247001 (2019).

[48] H. Sakakibara, H. Usui, K. Kuroki, R. Arita, and H. Aoki, Origin of the material dependence of  $t_c$  in the single-layered cuprates, *Phys. Rev. B* **85**, 064501 (2012).

[49] L. V. Boehnke, *Susceptibilities in Materials with Multiple Strongly Correlated Orbitals*, Ph.D. thesis, Universität Hamburg, Hamburg (2015).

[50] L. B. Braz, T. Nag, and A. M. Black-Schaffer, Competing magnetic states on the surface of multilayer abc-stacked graphene, *Phys. Rev. B* **110**, L241401 (2024).

[51] T. Löthman and A. M. Black-Schaffer, Universal phase diagrams with superconducting domes for electronic flat bands, *Phys. Rev. B* **96**, 064505 (2017).